J Nanopart Res (2013) 15:1837
DOI 10.1007/s11051-013-1837-5

RESEARCH PAPER

Nanosphere-Decorated Tunable Anatase Titania Conic Self-Assemblies

Bong June Zhang · Kwang Jin Kim · Deuk Yong Lee

Received: 8 April 2013 / Accepted: 3 July 2013 / Published online: 11 August 2013

Abstract The evolution of morphology has been a key parameter to modify electronic and physical properties of functional materials. For anatase titania, most research has been focused on tubular and/or mesoporous shapes. In this report, we note our findings of cone-shaped anatase titania self-assemblies grown by anodic oxidation. These individual anatase TiO_2 cones are constructed from numerous titania nanospheres. The variation in morphology (base diameter and height) is controlled by varying the electrolyte, the concentration of fluoride, and the applied voltage. The crystallization of the anatase phase and the enlarged surface area is confirmed by various spectroscopic methods (FE-SEM, EDS, and TEM). Through controlling the enhanced surface area and the well-ordered ion passage, the Li^+ diffusion rate significantly increases and leads to reversibility (charge–discharge cycle). The CV and EIS results imply structurally modified titania conic self-assemblies which can be a potential lithium intercalation template.

B. J. Zhang · K. J. Kim (✉)
Low Carbon Green Technology Laboratory, Department of Mechanical Engineering (MS312), University of Nevada, Reno, NV 89557, USA
e-mail: kwang.kim@unlv.edu

D. Y. Lee
Department of Convergence Biomedical Engineering/ Materials Engineering, Daelim University, 29, Imkok-Ro, Anyang 431-715, South Korea

Keywords Titanium dioxide · Morphology · Solution chemistry · Crystallinity · Electrochemistry

Introduction

The titania has attracted special attention due to its scientific and engineering aspects (self-cleaning (Fujishima and Honda 1972; Ng et al. 2008), photocatalyst (Sosnowchik et al. 2010; Castro et al. 2008), dye-sensitized solar cells (DSSCs) (Boercker et al. 2008; Pan et al. 2011; Chen et al. 2010), and energy storage (Poizot et al. 2000; Wang et al. 2008). These potential applications are arise from the unique physical and chemical properties of TiO_2, which are influenced by its crystal phase as well as morphology. Among the three crystal phases, anatase, rutile, and brookite, anatase is the only one found in nature and has the most efficient crystallographic structure to intercalate cations. The particle size and the shape of TiO_2 determine optical and electronic properties. There have been various uniquely-shaped structures: nanotubes (NTs) (Štengl et al. 2007; Kim et al. 2009, 2011; Albu et al. 2008; Mahajan et al. 2008), nanoparticles (NPs) (Wang et al. 2012; Meng et al. 2012; Kavan et al. 1995; Wei et al. 2007), *nanoflower* (Yang et al. 2011), and nanospheres (NSs) (Yu et al. 2011).

In respect of synthesis of the titania thin films, interdisciplinary approaches have been incorporated:

chemical vapor deposition (CVD) (Taylor et al. 1999; Krumdiek and Raj 1999), RF sputtering (Akl et al. 2006), sol–gel synthesis (Wang and Hu 1999; Verma and Agnihotry 2007), and anodizing (Albu et al. 2008; Kim et al. 2009). The anodic oxidation process has been considered as the most versatile technique because it is suitable for mass production and is capable of yielding large surface areas. Herein, we investigate an approach to form conical-shaped anatase TiO_2. This structure is composed of self-assembled anatase TiO_2 NPs and shows unique electrochemical properties (Reddy and Ramaprabhu 2007; Jung et al. 2010; Lu et al. 2010).

Experimental section

TiO_2 nano conic structure preparation and characterization

Titanium foil was obtained from Sigma-Aldrich (99.7 %, 0.127 mm thick) and used as it was received without further surface treatment. The Ti foil was cut into 1 cm × 4 cm and chemically cleaned in acetone and ethanol (1:1 by vol) under ultrasonication for ten minutes. Aqueous 1.0 M H_3PO_4 with 0.5 wt% NH_4F electrolytes was prepared. After the addition of the fluoride source to the solution, the mixture was stirred for 2 h to fully dissolve the salt at room temperature. The Ti specimen was then anodized in potentiostatic mode (10–100 V) at room temperature in the electrolytes. An Agilent N5771A DC power supply was used for all tests. After the anodization, specimens were thoroughly rinsed with ethanol followed by de-ionized water. Individual specimens were fully dried in the oven at 95 °C overnight. The microscopic morphology and structure observation were carried out using a field-emission scanning electron microscope (FE-SEM, Hitachi S-4700). Chemical elements were analyzed by electron dispersive spectroscopy (EDS, INCA Energy oxford instruments) on a scanning electron microscope. For cross-sectional view analysis, SEM images were taken using focused ion beam (FIB) milling technique. The dual beam FIB system was allowed for SEM images of the milled sample in the process chamber.

Electrochemical properties of TiO_2 nano conic structures

A typical three electrode (test sample, reference, counter electrode) system was used to determine the electrochemical impedance spectroscopy (EIS) and cyclic voltammetry (CV) measurements. A carbon rod and a saturated calomel electrode (SCE) were used for counter and reference electrodes, respectively. Working electrodes were prepared using Titanium foil (4 cm × 1 cm, thickness 0.127 mm). Anodized titanium foils described in "TiO_2 nano conic structure preparation and characterization" section were masked using an epoxy resin except for the exposed area (1 cm^2). Working electrodes were oven-dried at 95 °C for 24 h. An 1.0 M $LiClO_4$ solution was prepared for the electrolyte. A potentiostat (Voltalab 40 PCZ, Radiometer Copenhagen) was used for EIS and CV data acquisition. Before data acquisition, an individual test specimen was equilibrated in the electrolyte for 5 min. The scan frequency range of EIS was 10^5–10^2 Hz at a rate of 100 mV/s. The obtained EIS data were shown as Nyquist and Bode plots. For CV, the potential scan range was varied from −1.5 to +1.5 V (vs. SCE) with scan rates of 5–200 mV/s.

Results and discussion

Morphology and structure evolution of the TiO_2 nano cones

The titania nanospheres-decorated cones (TNC) were characterized by field-emission scanning electron microscopy (FE-SEM). Micrographs of FE-SEM in Fig. 1a show a tilted view of a single TNC. The TNC is tapered and consists of multitudinous ruffles. The TNC is vertically grown with respect to the substrate. Higher magnification of Fig. 1a reveals that numerous titania nano spheres (TNPs) are clearly observed on the individual ruffles as shown in Fig. 1b and it is assumed that the TNC is made of TNPs.

In order to elucidate the bottom-up growth of the TNC, series of time-elapsed morphology evolution micrographs using FE-SEM were taken over a period of 8 h under the following condition: anodization at 20 V in 1.0 M H_3PO_4 with 0.5 wt% NH_4F. Figure 2

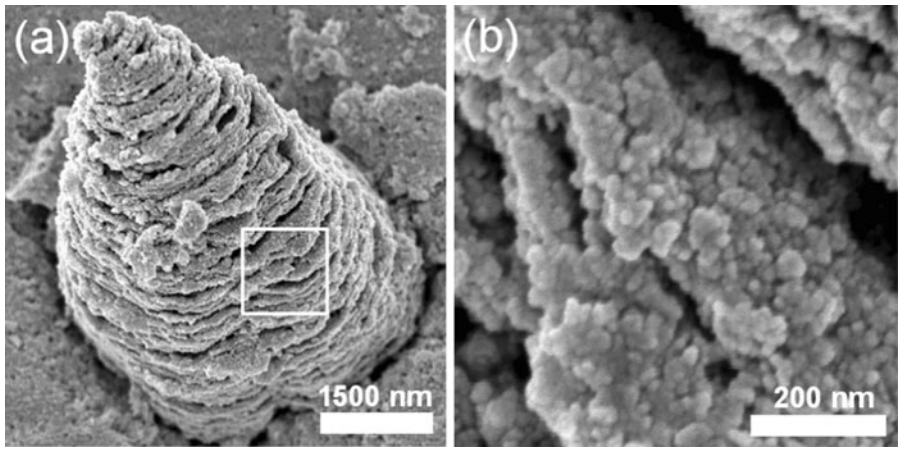

Fig. 1 FE-SEM images of titania nano cone (TNC) anodized at 40 V in 1.0 M H_3PO_4 with 0.5 wt% NH_4F: **a** Tilted view of TNC and **b** higher magnification of TNC ruffles represented in *square* in Fig. 1a decorated with titania nano sphere (TNS)

shows (a) the measured cone-diameter, (defined as the base diameter) versus the anodizing reaction time, and (b) the measured cone-diameter versus applied voltage, *V*. As illustrated in Fig. 2, the morphology evolution can be described as a two-step process. In the first phase (0.5 h), numerous TNSs, which are nucleated from a titanium substrate during the anodic oxidation process, are observed. The diameter of each TNS is approximately 20 nm (see Fig. 2, 0.5 h). In the second phase, the TNSs begin to form aggregates (1.0 h) as the anodizing process continues. Once these aggregates form, the individual TNSs build up the TNCs through a ruffle-layering phenomenon. After 2 h, the diameter reaches a plateau at approximately 1 μm while the individual TNCs continue to grow with an increase in the population density over the course of 8 h.

Other parameters were varied to observe if the structure of TiO_2 could be preferentially based on three structures, NTs, NPs, and NSs. The type of electrolytes (e.g., organic and aqueous), fluoride sources (NH_4F and HF), and voltage applied (Zhang and Kim 2012; Li et al. 1998) were varied. For an aqueous 1.0 M H_3PO_4 electrolyte with limited amount of fluoride (0.5 wt% NH_4F) added, the TiO_2 did not form NTs, but instead, NCs were constructed with NS aggregates formed on the substrate. The growth of the cone-diameter shows a linear proportionality to the applied voltage as seen in Fig. 2b. At 20 V, the diameter and height of the TNC (TNC20) are $\sim$1.2 and $\sim$3 μm, respectively. The population density of the TNC20 is $\sim 1.1/\mu m^2$. As the voltage increases, the size of the TNCs linearly increases, Fig. 2b, and the population density relatively decreases. At 60 V, the diameter and height of the TNC (TNC60) are $\sim$15 and $\sim$15 μm, respectively. The population density of the TNC60 decreases less than $\sim 0.06/\mu m^2$.

One thing to note in Fig. 2b is that TNC was not observed above 90 V. It should be pointed out that the amount of fluoride in the electrolyte has been previously shown to influence TNC formation (Zhang and Kim 2012; Li et al. 1998). In order to observe the influence of the catalytic amount of fluoride, TNC formation was tested over a wide fluoride concentration range (0.1–1.0 wt%), summarized in Table 1. These data supports the theory that TNC growth is stimulated by a fluoride-rich environment, which assists in the formation of the intermediate $[TiF_6]^-$ complex (Li et al. 1998). However, an excessive amount of fluoride is detrimental to the TNC growth at higher voltage regimes, causing accelerated chemical etching as shown in Table 1 (Zhang and Kim 2012; Li et al. 1998).

The chemical structure of the TNC is anodized at 20 V in an aqueous 1.0 M H_3PO_4 electrolyte solution with 0.5 % wt NH_4F (TNC20). The structure can be controlled by various methods such as FIB milling, transmission electron microscopy (TEM), and energy dispersive X-ray spectroscopy (EDS). Figure 3a shows an EDS analysis of the elemental composition of TNC20. EDS result in Fig. 3a reveals that there are an intensive titanium peak (kα 4.51 keV) and oxygen peak (kα 0.53 keV) at given surface area. The presence of TiO_2 is confirmed (Ti:O = 61:39 by wt%, 34:66 by at.%) by integrating peak area.

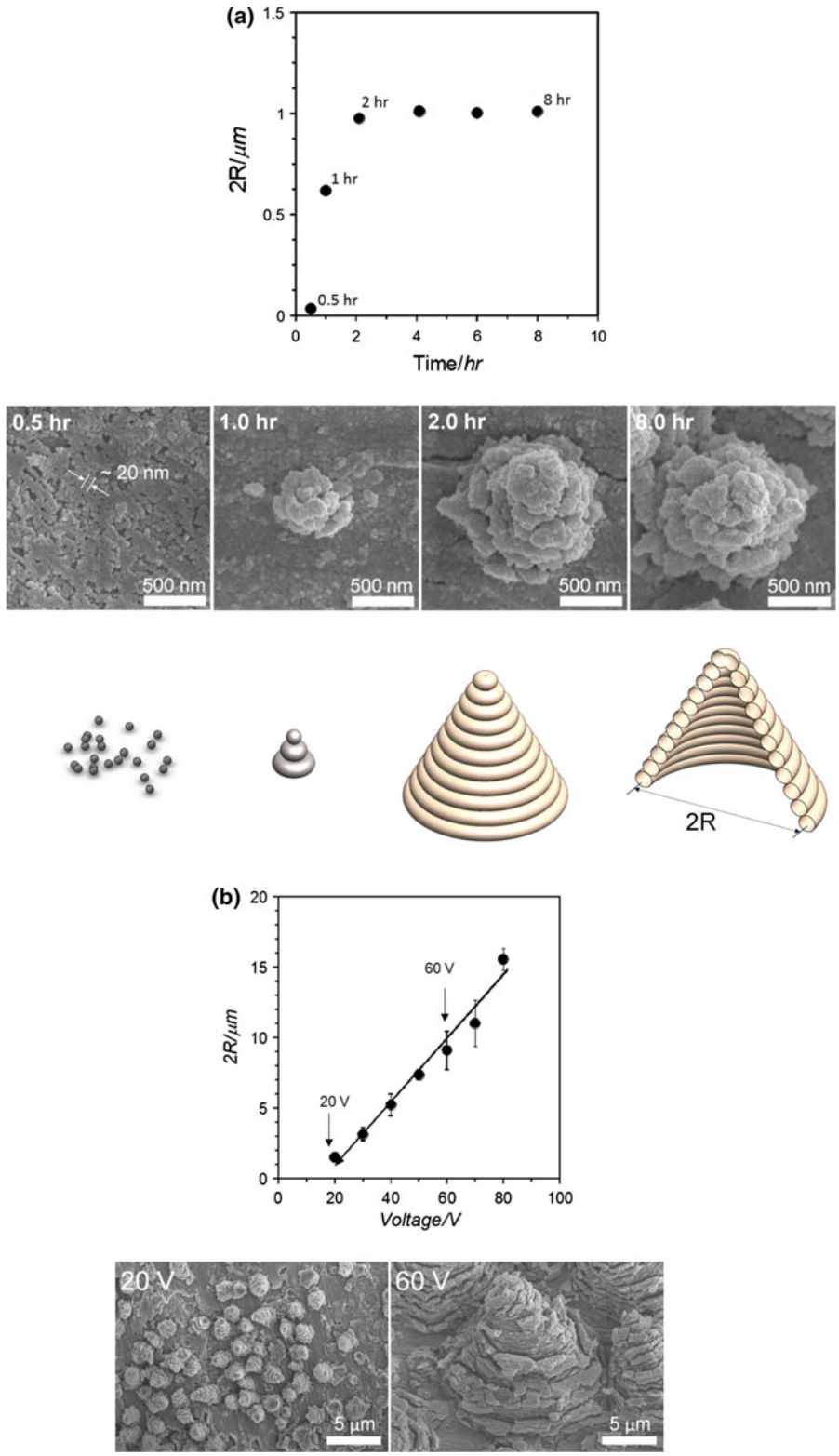

Fig. 2 **a** The measured cone-diameter versus anodizing reaction time and FE-SEM images and schematic illustration of the time-lapsed TNC evolutions from TNS: anodized at 20 V in 1.0 M H_3PO_4 with 0.5 wt% NH_4F for 8 h and **b** the measured cone-diameter versus anodizing voltage applied and FE-SEM images of TNC anodized at 20 and 60 V in 1.0 M H_3PO_4 with 0.5 wt% NH_4F for 8 h

Table 1 Anodizing results at different conditions (voltage/time/electrolyte)

Electrolyte	Fluoride concentration	Voltage (*V*)	Reaction time/h	Morphology
1.0 M H_3PO_4	0.1 wt% NH_4F	20	15	Cone
		40	15	Cone
		60	15	Cone
		80	15	Cone
	0.5 wt% NH_4F	20	15	Cone
		40	15	Cone
		60	15	Cone
		80	15	None
	1.0 wt% NH_4F	20	15	Cone
		40	15	Cone
		60	15	None
		80	15	None

Figure 3b shows a FE-SEM image of the cross-section of the TNC20, which is prepared by FIB milling. The image reveals that the inside of the conic structure is hollow and corrugated. The ruffles are clearly visible having a thickness of ~236 nm.

Figure 4a shows high resolution TEM (HR-TEM) images of the TNC20. A magnified image shows the polycrystalline of TiO_2. Inset of Fig. 4a shows lattice fringes separated by ~3.6 Å. In HR-TEM images, the lattice planes of anatase TiO_2 are oriented nearly perpendicular to the local nano cone axis. Careful examination of the angle between the lattice planes reveals that angle varies from ~90° to ~60°. Figure 4b shows the ring pattern from selected area electron diffraction (SAED). The electron diffraction pattern of the TNC20 (see Table 2) could be indexed to the anatase phase of TiO_2 (JCPDS-21-1272).

Electrochemical properties of TiO_2 nano cones

In order to understand the electrochemical nature of the TNC, CV was performed in 1.0 M $LiClO_4$ at room temperature with a potentiostat (Voltalab 40 PCZ, Copenhagen). The potential scan range was from −1.5 to +1.5 V (vs. SCE) with scan rates of 5–200 mV/s. The TNC specimens grown at 20 and 60 V were scanned at 200 mV/s. As seen in Fig. 5, the cyclic voltammograms show similar trends as the previous studies (Janáky et al. 2010; Dong et al. 2010; Kim et al. 2010) but a more significant peak and area difference between oxidation and reduction. The smooth curves in the cyclic voltammogram indicate that the TNC electrode layer is well-attached to the substrate. Both TNC specimens (TNC20/60) show a reasonably stable electrochemical reaction with the electroactive probe molecule, $LiClO_4$, in the electrolyte. Thus, TNCs

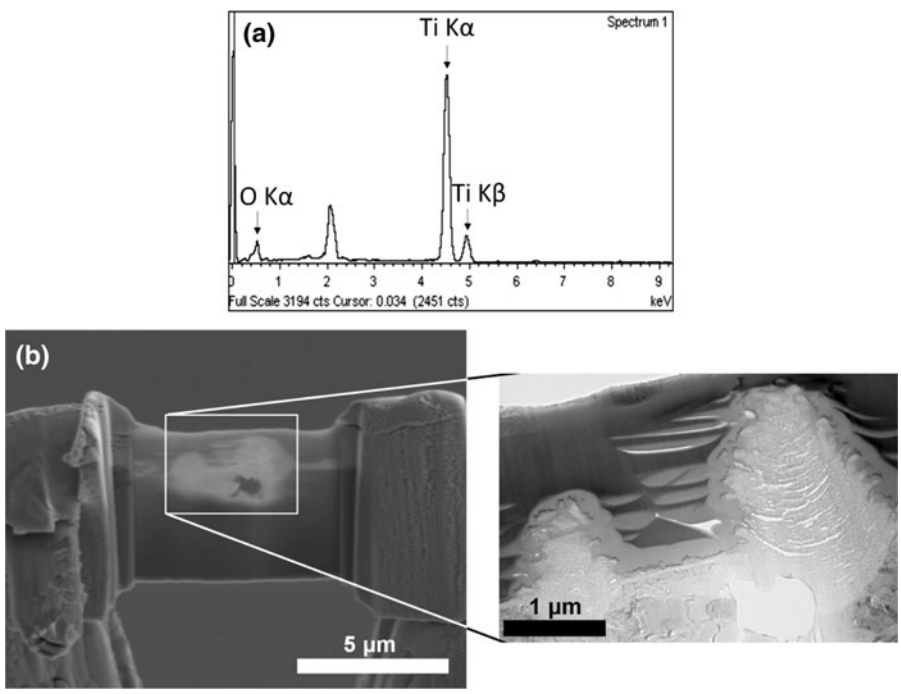

Fig. 3 TNC20 (anodized at 20 V in 1.0 M H_3PO_4 with 0.5 wt% NH_4F) spectroscopic structure analysis: **a** EDS elemental analysis. Ti:O = 61:39 by wt%, 66:34 by at.% and **b** FE-SEM image of the focused ion beam (FIB) milled specimen. *Inset* shows cross-section of TNC 20

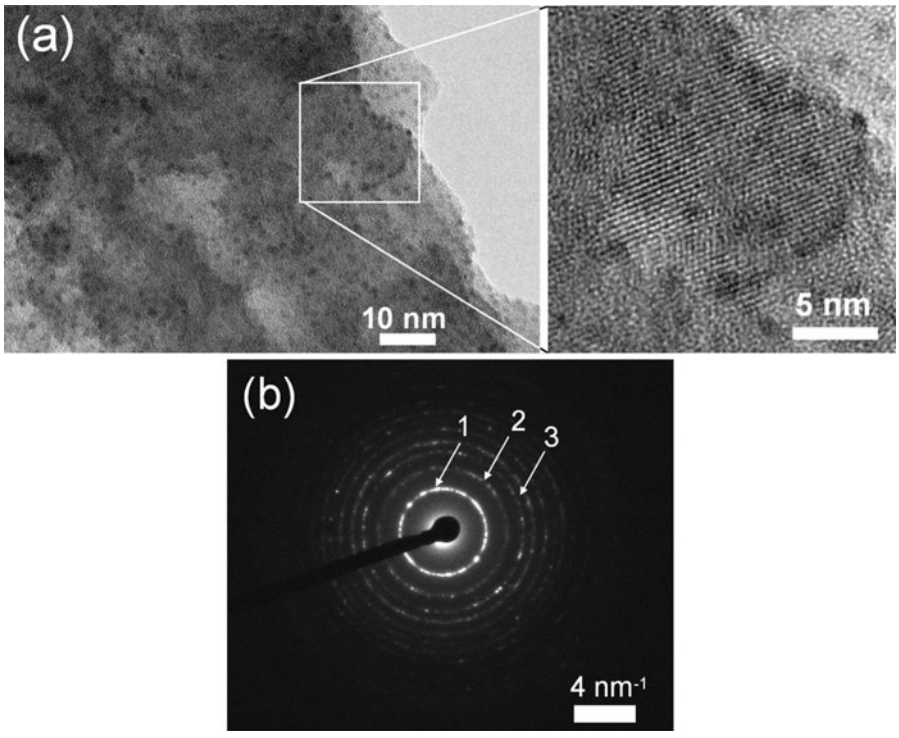

Fig. 4 TNC20 (anodized at 20 V in 1.0 M H_3PO_4 with 0.5 wt% NH_4F) spectroscopic structure analysis: **a** HR-TEM image. *Inset* shows polycrystalline TiO_2 nano cone and **b** SAED pattern from TiO_2 nano cones which can be indexed to anatase TiO_2. See *d*-spacing instead in Table 2 which corresponds to individual labels in Fig. 4b

Table 2 *d*-Spacing measurements by using TEM

Layer	1/nm	*d*-spacing (nm)
1	5.534	0.361402
2	8.278	0.241604
3	10.341	0.193405

properly function as an effective host matrix for the intercalation of Li^+. The integrated area of the cyclic voltammogram of the TNC60 is 49 % larger than that of TNC20 (Fig. 5). This finding indicates that larger electron transfer (ET) rates and electrochemical activity occur due to the larger exposed surface area (Verma and Agnihotry 2007). Each conic structure, which is decorated with a large number of the NPs, can facilitate lithium adsorption on the surface. This adsorption is probably due to the formation of the continuous and well-ordered pathway of Li^+.

In order to confirm adhesion strength of the TNC, electrode bending test was also performed. As shown in Fig. 5a, the TNC electrode surface remains intact even at extreme bending. On the contrary, the titania NT (TNT) electrode, anodized at 30 V in glycerol with 3 wt% NH_4F, shows not only flaking along the edge (arrowed area), but also a large area delamination on the back in Fig. 5b. For a quantitative analysis of the adhesion strength of the TNC electrode to the substrate, a cross-cut adhesion test (ASTM D 3359) was carried out. As shown in Fig. 6, TNC60 (1.5×1.5 cm^2) electrode, anodized at 60 V in an aqueous 1.0 M H_3PO_4 electrolyte solution with 0.5 wt% NH_4F was prepared. The electrode surface was cut and extracted using adhesive tape. In general, the adhesion test results are categorized into six different levels based on the detached surface area (6: no failure—0: greater than 65 % area). As shown in Fig. 6a, there is no significant adhesion failure observed with bare eyes. In order to confirm adhesion strength at microscale, the electrode surface was magnified by a digital microscope (Keyence VHX-2000). Even at higher magnification (200 times magnification), no significant delamination and/or no adhesion failure was observed even at edge in Fig. 6b.

In order to understand the diffusion behavior of lithium cations (Li^+) in the TNC, cyclic voltammograms of the TNC20 and the TNC60 were measured in 1.0 M $LiClO_4$ at different scan rates (5–200 mV/s) in Fig. 7a, b. The peak current densities, i_p, of the TNCs at each scan rate were plotted using the Randles–Sevcik

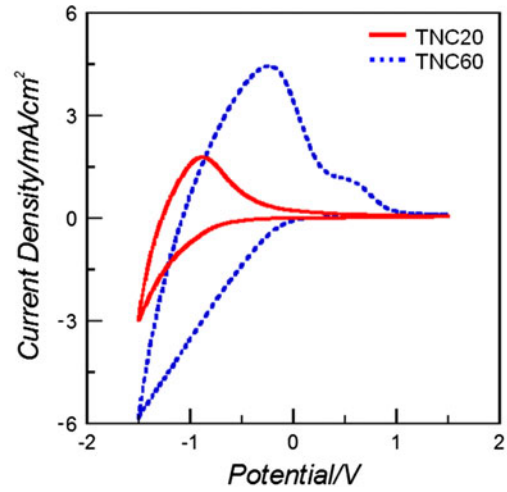

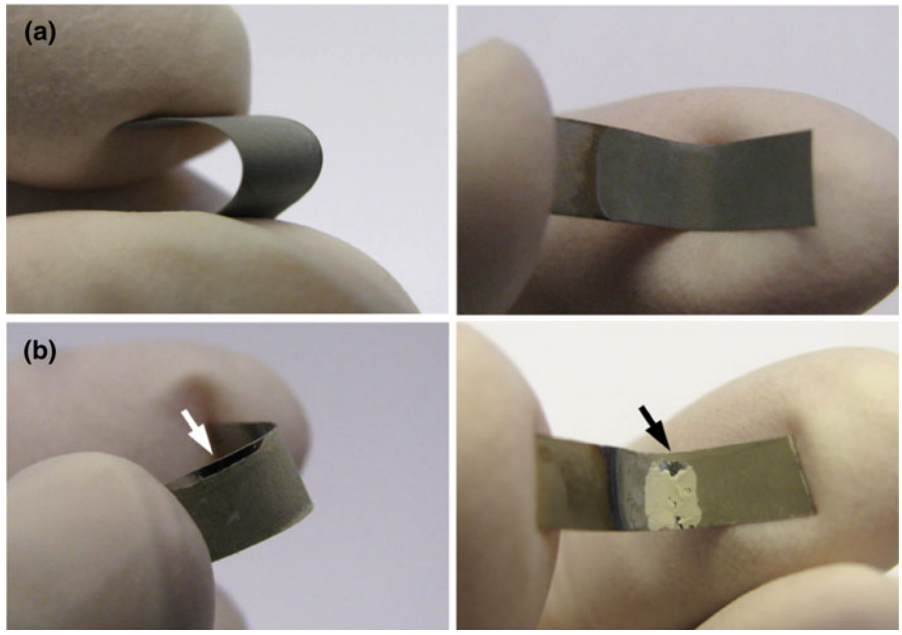

Fig. 5 Cyclic voltammograms of the TNC20 (anodized at 20 V) and the TNC60 (anodized at 60 V) in 1.0 M LiO_4. Scan rate 200 mV/s. Bending test: **a** the TNC electrode and **b** the TNT electrode. Metal substrate (indicated by the *arrow*) is shown along the edge of the electrode

equation shown in Eq. (1), which can be use to compare the diffusion rates of the lithium cation in the TNCs (Chen et al. 2011):

$$i_p = (2.69 \times 10^5) v^{1/2} n^{3/2} A D_a^{1/2} C \quad (1)$$

where i_p is the peak current density, v is scan rate, n is the number of electrons in the reaction, A is the electrode area, and C is concentration.

The results are shown in Fig. 7a, b insets. Observing the plot in Fig. 7a, the peak current density at lower scan rate region (<56.5 mV/s) seems to be linearly proportional to the scan rate for TNC20 (Bard et al. 1980). This finding indicates that the relative diffusion rate, with respect to that of mass transport, is sufficient to maintain the Nernstian equilibrium at the electrode surface. Therefore this suggests that the Li^+ intercalation is reversible reactions with the TNC20 electrode subjected to charge–discharge cycles (Yang et al. 2011; Brett and Brett 1993; Meekins and Kamat 2009). On the contrary, for TNC60, the linearity is limited to lower scan rate (reversible). As scan rate increases, peak current density deviates from linearity.

The diffusion coefficient, D_a, at different scan rates is tabulated in Table 3 using the Randles–Sevcik equation (Wei et al. 2007). At a lower scan rate (<56.5 mV/s), D_a of TNC60 is almost twice the

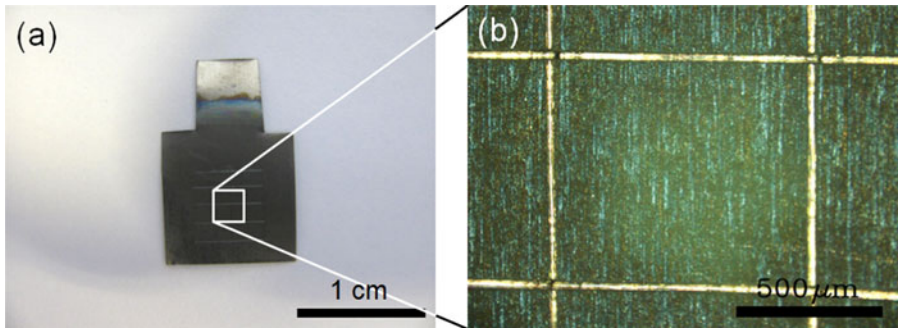

Fig. 6 **a** Mechanical adhesion test specimen and **b** *inset* shows the high magnification image of cross-cut of the TNC60

number of the TNC20. The significantly enhanced diffusion rate of the TNC60 is presumably due to its structural uniqueness. The TNC60 shows a greatly enhanced hollow surface area with an evenly distributed wall thickness of ~150 nm. This thickness enables the Li^+ to diffuse in and out with greater ease than TNC20. On the contrary, the TNC20, in Fig. 3b inset, shows a partially filled cone shape with a wall thickness of ~256 nm, hampering Li^+ diffusion due to the longer passage way.

Furthermore, EIS was carried out with $LiClO_4$ as the electrolyte at room temperature because EIS has been regarded as powerful technique to examine charge carrier transport and recombination process in DSSCs. The frequency was swept from 10 mHz to 100 kHz with an applied voltage of 0.18 V (vs. SCE). Figure 8a, b shows the Nyquist plots (Pan et al. 2011) at the different frequency regimes (Fabregat-Santiago et al. 2002). In the Nyquist plots, the high frequency semicircle portion corresponds to the reduction reaction at the counter electrode and the low frequency second semicircle is assigned to charge transfer at the TiO_2/electrolyte interface (Conway 1999; Bernard et al. 2003). The diameter of the semicircle of the TNC20 is approximately two times larger than that of the TNC60. The pronounced semicircle of the TNC20 indicates that charge transfer, at the low frequency domain, is more impeded compared to the TNC60. The TNC20 in Fig. 3b has a much thicker wall thickness and partially filled cone, which both play a role of a conductive barrier; however, the TNC60 has a facile conductive pathway arising from a thinner wall and shows an enhanced conductivity to the substrate. This result readily agrees with the CV results from Fig. 7a, b. The EIS at the high frequency regime is also presented in Fig. 8b. Each Nyquist plot, in the high frequency domain, shows an ohmic resistance and electrochemical double layer (EDL) impedance (Wang et al. 2008). It should be noted that both of the TNC electrodes are unique in exhibiting low ohmic resistance and EDL impedance (Wei et al. 2007). The initiation of the lithium intercalation occurs at 0.43 and 0.93 mΩ for

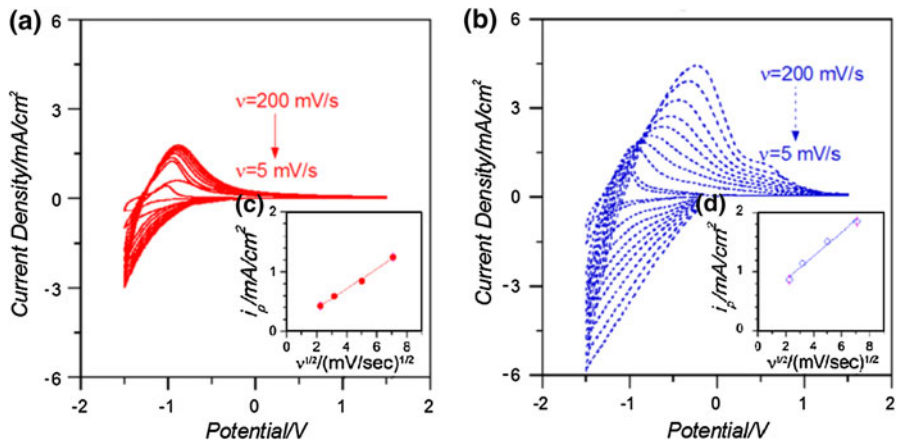

Fig. 7 Cyclic voltammograms (CVs): **a** TNC20 and **b** TNC60 in 1.0 M $LiClO_4$ at different scan rates (200–5 mV/s). *Insets* show Randles–Sevcik plots: *c* TNC20 and *d* TNC60 at different scan rates

Table 3 Calculated current density, scan rate, and diffusion coefficient based upon the Randles–Sevcik equation

Electrode	Current density I_p (mA/cm^2)	Scan rate V (mV/s)	Diffusion coefficient D_a (10^{-9} cm^2/s)
TNC20	0.426	5	0.50
	0.594	10	0.49
	0.845	25	0.39
	1.25	50	0.43
TNC60	0.87	5	2.09
	1.15	10	1.83
	1.42	25	1.11
	1.85	50	0.95

TNC20 and TNC60, respectively. Figure 8c, d shows different Bode plots with respect to the capacitance and phase of the fabricated TNCs. The capacitance of the TNC60 was approximately three times larger than that of the TNC20, as seen in Fig. 8c. Considering the capacitance of a typical EDL is 20 μF/cm (Mahajan et al. 2008), the capacitance of the TNC60 was dramatically improved. In general, the frequency shift in the Bode plot is related to the inverse of the recombination lifetime or electron lifetime in the TiO_2 network. The phase angle of the TNC60 was linear with respect to frequency, Fig. 8d. However, the phase angle of the TNC20 showed large deviation at approximately 100 Hz. The large phase angle change at a relatively high frequency regime implies that the collection and transportation of electrons in the TNC20 is longer than that of the TNC60. This phenomenon can be ascribed to the intercalated Li^+ concentration in the TNC electrode. Combined with the diffusion coefficient obtained by the Randles–Sevcik equation in Table 3, the EIS results appear consistent with each other.

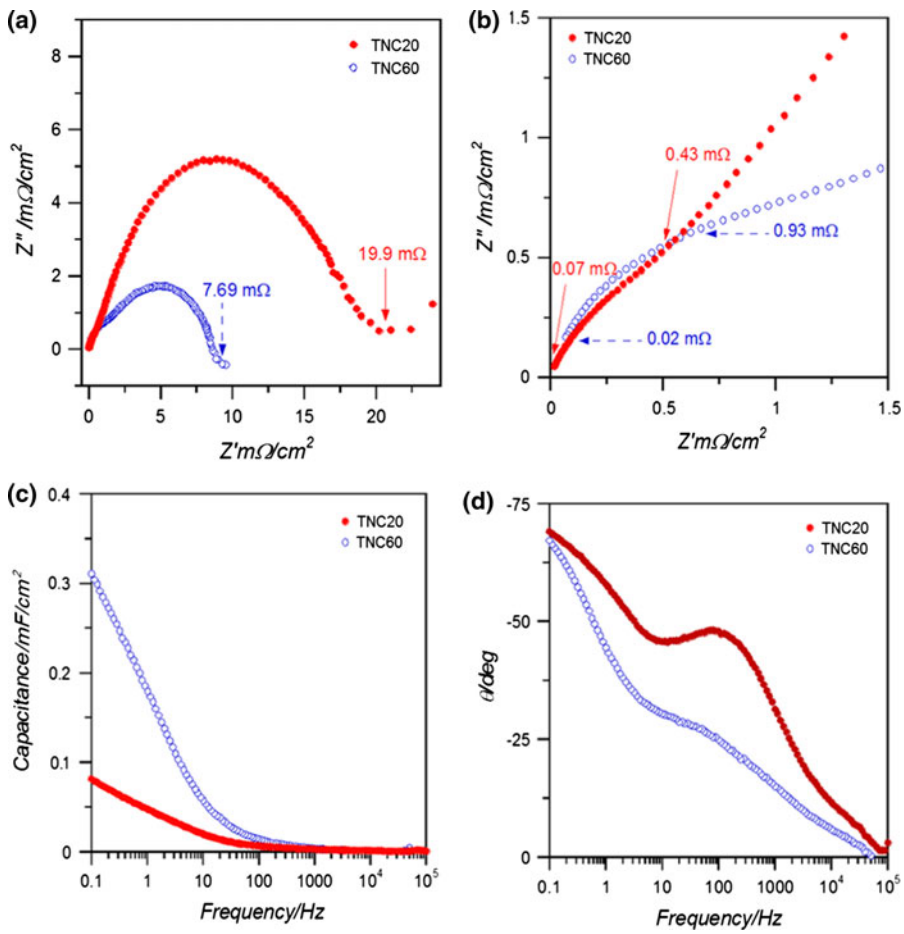

Fig. 8 Nyquist plots of EIS: **a** TNC20 and **b** TNC60 at different frequency regimes. Bode plots of EIS: **c** capacitance and **d** phase of TNC20 and TNC60

Conclusions

In summary, hollow conical anatase TiO_2 could be controllably created on Ti foils by anodic oxidation by carefully controlling parameters such as the type of electrolytes, voltage, and fluoride. From the electrochemical analysis, the intercalated Li^+ storage-ability is closely related to the enhanced surface area and the continuous, well-ordered Li^+ passage. In addition, the remarkably larger diffusion coefficient for Li^+ emphasizes the importance of a facile conductive pathway to the electrode. This diffusion leads to lithium intercalation reversibility since the electrode is subjected to a charge–discharge cycle.

Acknowledgments The authors acknowledge the partial financial support from the U.S. Department of Energy

References

Akl AA, Kamal H, Abdel-Hady K (2006) Fabrication and characterization of sputtered titanium dioxide films. Appl Surf Sci 252(24):8651–8656. doi:10.1016/j.apsusc.2005.12.001

Albu SP, Kim D, Schmuki P (2008) Growth of aligned TiO_2 bamboo-type nanotubes and highly ordered nanolace. Angew Chem Int Ed 47(10):1916–1919. doi:10.1002/anie.200704144

Bard AJ, Larry R, Faulkner R (1980) Electrochemical methods: fundamentals and applications. Wiley, New York

Bernard MC, Cachet H, Falaras P, Hugot-Le Goff A, Kalbac M, Lukes I, Oanh NT, Stergiopoulos T, Arabatzis I (2003) Sensitization of TiO_2 by polypyridine dyes: role of the electron donor. J Electrochem Soc 150(3):E155–E164. doi:10.1149/1.1543951

Boercker JE, Enahce-Pommer E, Aydil ES (2008) Growth mechanism of titanium dioxide nanowires for dye-sensitized solar cells. Nanotechnology 19(9):095604. doi:10.1088/0957-4484/19/9/095604

Brett CMA, Brett AMO (1993) Electrochemistry: principles, methods, and applications. Oxford University Press, New York

Castro MRS, Sam ED, Veith M, Oliveira PW (2008) Structure, wettability and photocatalytic activity of CO_2 laser sintered TiO_2/multi-walled carbon nanotube coatings. Nanotechnology 19(10):105704. doi:10.1088/0957-4484/19/10/105704

Chen J, Chen C, Wu C, Lin C, Lai Y, Wang C, Chen H, Vittal R, Ho K (2010) An efficient flexible dye-sensitized solar cell with a photoanode consisting of TiO_2 nanoparticle-filled and SrO-coated TiO_2 nanotube arrays. J Mater Chem 20(34):7201–7207. doi:10.1039/C0JM00598C

Chen R, Hu L, Huo K, Fu J, Ni H, Tang Y, Chu PK (2011) Controllable growth of conical and cylindrical TiO_2-carbon core-shell nanofiber arrays and morphologically dependent electrochemical properties. Chem Eur J 17:14552–14558. doi:10.1002/chem.201102219

Conway BE (1999) Electrochemical supercapacitors: scientific fundamentals and technological applications. Kulwar Academic Press/Plenum Publisher, New York

Dong B, He B, Chai Y, Liu C (2010) Novel Pt nanocluster/titanium dioxide nanotubes composites for hydrazine oxidation. Mater Chem Phys 120(2–3):404–408. doi:10.1016/j.matchemphys.2009.11.022

Fabregat-Santiago F, Garcia-Belmonte G, Bisquert J, Zaban A, Salvador P (2002) Decoupling of transport, charge storage, and interfacial charge transfer in the nanocrystalline TiO_2/electrolyte system by impedance methods. J Phys Chem B 106(2):334–339. doi:10.1021/jp0119429

Fujishima A, Honda K (1972) Electrochemical photolysis of water at a semiconductor electrode. Nature 238:37–38. doi:10.1038/238037a0

Janáky C, Bencsik G, Rácz Á, Visy C, De Tacconi NR, Chanmancee W, Rajeshwar K (2010) Electrochemical grafting of poly(3,4-ethylenedioxythiophene) into a titanium dioxide nanotube host network. Langmuir 26(16):13697–13702. doi:10.1021/la101300n

Jung I, Choi J, Tak Y (2010) Nicekl oxalate nanostructures for supercapacitors. J Mater Chem 20(29):6164–6169. doi:10.1039/C0J00279H

Kavan L, Kratochvilová K, Grätzel M (1995) Study of nanocrystalline TiO_2 (anatase) electrode in the accumulation regime. J Electroanal Chem 394(1–2):93–102. doi:10/1016/0022-0728(95)03976-N

Kim D, Lee K, Roy P, Birajdar BI, Spiecker E, Schmuki P (2009) Guanidinium-modified phthalocyanines as high-affinity G-quadruplex fluorescent probes and transcriptional regulators. Angew Chem Int Ed 48(49):9362–9365. doi:10.1002/anie.200903685

Kim J, Zhu K, Yan Y, Perkins CL, Frank AJ (2010) Microstructure and pseudocapacitive properties of electrodes constructed of oriented NiO–TiO_2 nanotube arrays. Nano Lett 10(10):4099–4104. doi:10.1021/nl102203s

Kim JY, Sekino T, Park DJ, Tanaka SI (2011) Morphology modification of TiO_2 nanotubes by controlling the starting material crystallite size for chemical synthesis. J Nanopart Res 13:2319–2327. doi:10.1007/s11051-010-9990-6

Krumdiek S, Raj R (1999) Conversion efficiency of alkoxide precursor to oxide films grown by an ultrasonic-assisted, pulsed liquid injection, metalorganic chemical vapour deposition (pulsed-CVD) process. J Am Ceram Soc 82(6):1605–1607. doi:10.1111/j.1151-2916.1999.tb01969x

Li F, Zhang L, Metzger RM (1998) On the growth of highly ordered pores in anodized aluminum oxide. Chem Mater 10(9):2470–2480. doi:10.1021/cm980163a

Lu L, Zhu Y, Li F, Zhuang W, Chan KY, Lu X (2010) Carbon titania mesoporous composite whisker as stable supercapacitor electrode material. J Mater Chem 20(36):7645–7651. doi:10.1039/C0JM00054J

Mahajan VK, Misra M, Raja KS, Mohapatra SK (2008) Self-organized TiO_2 nanotubular arrays for photoelectrochemical hydrogen generation: effect of crystallization and defect structures. J Phys D 41(12):125307. doi:10/1088/0022-3727/41/12/125307

Meekins BH, Kamat PV (2009) Got TiO_2 nanotubes? Lithium ion intercalation can boost their photoelectrochemical performance. ACS Nano 3(11):3437–3446. doi:10.1021/nn900897r

Meng X, Qi L, Xiao Z, Gong S, Wei Q, Liu Y, Yang M, Wang F (2012) Facile synthesis of direct sunlight-driven anatase TiO_2 nanoparticles by in situ modification with trifluoroacetic acid. J Nanopart Res 14:1176. doi:10.1007/s11051-012-1176-y

Ng CJW, Gao H, Tan TTY (2008) Atomic layer deposition of TiO_2 nanostructures for self-cleaning applications. Nanotechnology 19(44):445604. doi:10.1088/0957-4484/19/44/445603

Pan X, Chen C, Zhu K, Fan Z (2011) TiO_2 nanotubes infiltrated with nanoparticles for dye sensitized solar cells. Nanotechnology 22(23):235402. doi:10.1088/0957-4484/22/23/235402

Poizot P, Laruelle S, Grugeon S, Dupont L, Tarascon JM (2000) Nano-sized transition-metal oxides as negative-electrode materials for lithium-ion batteries. Nature 407(6803):496–501. doi:10.1038/35035045

Reddy ALM, Ramaprabhu S (2007) Nanocrystalline metal oxides dispersed multiwalled carbon nanotubes as supercapacitor electrodes. J Phys Chem C 111(21):7727–7734. doi:10.1021/jp069006m

Sosnowchik BD, Chiamori HC, Ding Y, Ha J, Wang ZL, Lin L (2010) Titanium dioxide nanoswords with highly reactive, photocatalytic facets. Nanotechnology 21(48):485601. doi:10.1088/0957-4484/21/48/485504

Štengl V, Bakardjieva S, Murafa N, Večerniková E, Šubrt J, Balek V (2007) Preparation and characterization of titania based nanowires. J Nanopart Res 9:455–470. doi:10.1007/s11051-006-9125-2

Taylor CJ, Gilmer DC, Colombo DG, Wilk GD, Campbell SA, Roberts J, Gladfelter WL (1999) Does chemistry really matter in the chemical vapour deposition of titanium dioxide? Precursor and kinetic effects on the microstructure of polycrystalline films. J Am Chem Soc 121(22):5220–5229. doi:10.1021/ja984446f

Verma A, Agnihotry SA (2007) Thermal treatment effect on nanostructured TiO_2 films deposited using diethanolamine stabilized precursor sol. Electrochim Acta 52(7):2701–2709. doi:10.1016/j.electacta.2006.09.036

Wang Z, Hu X (1999) Fabrication and electrochromic properties of spin-coated TiO_2 thin films from peroxo-polytitanic acid. Thin Solid Films 352(1):62–65. doi:10.1016/S0040-6090(99)00321-1

Wang D, Fang H, Li F, Chen Z, Zhong Q, Qing G, Cheng H (2008) Aligned titania nanotubes as an intercalation anode material for hybrid electrochemical energy storage. Adv Funct Mater 18(23):3787–3793. doi:10.1002/adfm.200800635

Wang Y, Gao B, Morales VL, Tian Y, Wu L, Gao J, Bai W, Yang L (2012) Transport of titanium dioxide nanoparticles in saturated porous media under various solution chemistry conditions. J Nanopart Res 14:1095. doi:10.1007/s11051-012-1095-y

Wei T, Wan C, Wang Y, Chen C, Shiu H (2007) Immobilization of poly(n-vinyl-2-pyrrolidone)-capped platinum nanoclusters on indium-tin oxide glass and its application in dye-sensitized solar cells. J Phys Chem C 111(12):4847–4853. doi:10.1021/jp067501c

Yang X, Jin C, Liang C, Chen D, Wu M, Yu JC (2011) Nanoflower arrays of rutile TiO_2. Chem Commun 47:1184–1186. doi:10.1039/c0cc04216a

Yu IG, Kim YJ, Kim HJ, Lee C, Lee WI (2011) Size-dependent light-scattering effects of nanoporous TiO_2 spheres in dye-sensitized solar cell. J Mater Chem 21:532–538. doi:10.1039/C0JM02606A

Zhang BJ, Kim K (2012) Anodic-biased titania nanotube growth in low-dielectric viscous media. Int J Smart Nano Mater. i-print: 1–8. doi:10.1080/19475411.2012.662537